Motion Quantification and Automated Correction in Clinical RSOM

Juan Aguirre, Andrei Berezhnoi, Hailong He, Mathias Schwarz, Benedikt Hindelang, Murad Omar, and Vasilis Ntziachristos

***Abstract*— Raster-scan optoacoustic mesoscopy (RSOM) offers high-resolution non-invasive insights into skin pathophysiology, which holds promise for disease diagnosis and monitoring in dermatology and other fields. However, RSOM is quite vulnerable to vertical motion of the skin, which can depend on the part of the body being imaged. Motion correction algorithms have already been proposed, but they are not fully automated, they depend on anatomical segmentation pre-processing steps that might not be performed successfully, and they are not site-specific. Here, we determined for the first time the magnitude of the micrometric vertical skin displacements at different sites on the body that affect RSOM. The quantification of motion allowed us to develop a site-specific correction algorithm. The algorithm is fully automated and does not need prior anatomical information. We found that the magnitude of the vertical motion depends strongly on the site of imaging and is caused by breathing, heart beating, and arterial pulsation. The developed algorithm resulted in more than 2-fold improvement in the signal-to-noise ratio of the reconstructed images at every site tested. Proposing an effective automated motion correction algorithm paves the way for realizing the full clinical potential of RSOM.**

***Index Terms*— Dermatology, imaging, microvasculature, optoacoustic, photoacoustic, motion correction.**

I. Introduction

RASTER-SCAN optoacoustic mesoscopy (RSOM) is a optoacoustic (photoacoustic) imaging technique capable of visualizing tissue morphology and pathophysiological biomarkers of inflammatory and connective tissue diseases through several millimeters of depth while preserving high resolution [1]–[5]. Moreover, it can provide unique functional and molecular imaging of the skin [6]. Current RSOM systems can visualize primarily melanin and hemoglobin, which makes them well suited for characterizing microvascular structure and function as well as melanin-enriched structures. Other optoacoustic implementations can image the distribution of melanin and hemoglobin in tissue [7], [8] but they operate with transducers at lower frequencies and bandwidths and therefore they are not tailored to image the details of the smallest microvascular structures.

RSOM image formation is achieved by raster-scanning a focused ultrasound detector over the region of interest (ROI) to collect optoacoustic waves generated in the tissue in response to pulsed laser illumination. The focal point of the ultrasound detector lies slightly above the surface of the sample, and the detector collects ultrasound signals over an acceptance angle (aperture) defined by the focusing characteristics of the detecting element. At each detector position an "amplitude mode" line (A line) is obtained that allows the combination of several two-dimensional (2D) planes or "brightness mode" planes ("B-planes"), leading to a 3D sinogram that represents the detected optoacoustic wavefront. The collected data are tomographically reconstructed to yield an image that represents the 3D distribution of absorbed light within the skin [9]. The reconstruction algorithm assumes that a point detector is located at the focal point of the transducer, and that the detector accepts signals only within a cone that has an opening angle defined by the numerical aperture of the transducer [9].

Data acquisition speed is determined by the pulse repetition rate of the laser, which cannot exceed the limits imposed by laser safety regulations to avoid excessive light energy deposition in the skin [10]. Generally, RSOM acquisitions last around 1 minute. During this time, the subject's movement, due for example to breathing, can alter the position of the ultrasound detector relative to the sample, affecting RSOM image quality [11], [12].

Motion correction in RSOM was first introduced by Schwarz *et al.* [11]. In this initial work it was shown how vertical motion of the area to be imaged generates disruptions in the detected wave front. A motion correction algorithm was introduced that relied on segmentation of the skin's melanin layer in the three-dimensional sinogram, from which the disruptions could be quantified and corrected. The algorithm assumes the motion to be rigid. However, the quantity of the motion was not studied. If the amount of motion is

Manuscript received July 20, 2018; revised October 9, 2018 and November 15, 2018; accepted November 15, 2018. Date of publication January 24, 2019; date of current version May 31, 2019. This work was supported in part by the European Union's Horizon 2020 Research and Innovation Programme under Grant 687866 (INNODERM) and in part by the European Research Council (ERC) through the European Union's Horizon 2020 Research and Innovation Programme under Grant 694968 (PREMSOT). *(Corresponding author: Vasilis Ntziachristos.)*

J. Aguirre, A. Berezhnoi, H. He, M. Schwarz, M. Omar, and V. Ntziachristos are with the Institute of Biological and Medical Imaging, Helmholtz Zentrum Munich, D-85764 Neuherberg, Germany, and also with the Chair for Biological Imaging, Technical University Munich, D-81675 Munich, Germany (e-mail: v.ntziachristos@tum.de).

B. Hindelang is with the Department of Dermatology and Allergy, Technische Universität München, 80333 Munich, Germany.

Color versions of one or more of the figures in this paper are available online at http://ieeexplore.ieee.org.

Digital Object Identifier 10.1109/TMI.2018.2883154

too large, the non-rigid components of the displacements may prevent the algorithm to work correctly. Such motion poses a problem for RSOM analysis and it may explain the lack of success so far in imaging the back of the torso, which is clinically important because most melanomas develop there [13]. Therefore the motion correction algorithm should be tailored to the amount of motion present at a specific site on the body. The algorithm developed by Schwarz et al is also limited by the need for sufficient melanin to generate a detectable optoacoustic signal. Also, this algorithm is not automated, since segmentation of the melanin layer is not a straightforward process.

Here we hypothesized that understanding and measuring the vertical skin displacements at different skin areas may lead to improved motion correction algorithms for RSOM. Furthermore we hypothesized that the disruptions in the sinogram caused by motion should affect the cross-correlation function between A-lines or B-planes. If so, then it should be possible to correct for motion fully automatically without anatomical segmentation.

To test these hypotheses, we measured the micrometric vertical skin displacements at different skin areas that affect RSOM. We studied for the first time the origin and magnitude of the skin vertical displacements. Using such information we developed an automated motion correction algorithm. We quantified the improvement in RSOM image quality at different sites of the body achieved by applying the algorithm.

II. Methods

A. Measuring the Vertical Motion of the Skin

We created a method to measure the vertical motion of the skin using the hardware elements contained in RSOM. Instead of raster-scanning the transducer in the usual fashion, we held the RSOM scan head fixed at the desired body location and optoacoustic signals were collected for 10 sec. The repetition rate of the laser (500 Hz) was the same as that in a regular RSOM imaging session. In this way, a 1D signal was collected for each laser pulse. All the 1D signals were assembled next to one another to build a 2D plane, allowing motion to be observed. We termed these planes "motion graphs" (Fig 1).

Since the illumination wavelength was 532 nm, the amplitude of the 1D signal was high when the transducer sensed the part of the wavefront generated at the melanin layer in the stratum basale and the microvessels in the different areas of the dermis. Therefore, the motion graphs were capturing the vertical displacements of the stratum basale and microvessels. By calculating the position of the maximum of the cross-correlation function between the first 1D signal and the remaining 1D signals, one can calculate a displacement function, DF (m):

$$DF(\tau) = \text{argmax}_{vt}(A(0, vt) * A(\tau, vt)) \quad (1)$$

where $A(\tau, vt)$ is a 1D signal (V) acquired at the time point τ (s); v (m/s) is the speed of ultrasound in water; t is the time (s) needed for the optoacoustic signal to travel from its origin to the detector (see Fig 1a); vt (m) is the reciprocal distance; and * is the cross-correlation operator.

We calculated the displacement function for the following areas of the body on 3 healthy volunteers: lower limb, upper limb, forearm, upper arm, chest, back and wrist. We also measured on the chest area above the heart, at the so-called Erb's point [14], while subjects held their breath, in order to avoid breathing motion and capture only motion due to heart beating. We defined the mean motion for a certain area as the mean of the peak-to-peak distances in the DF graphs for all the measured subjects.

We performed our investigations using the RSOM55 set-up, which is so far the most versatile RSOM type. It is based on a 55 MHz transducer capable of capturing signals with frequency components ranging from 10 MHz to 120 MHz (Sonaxis, Besancon, France [15]). RSOM55 can image the whole range of microvessels that make up the microvascular structure (capillaries, venules, arterioles). The system architecture and components have been described elsewhere [3]. The illumination source is a 532-nm ND:YAG laser (Wedge, Bright Solutions, Italy) with a pulse width around 1 ns. The acquired signals were divided into two frequency bands: 10–42 MHz (low) MHz and 42–120 MHz (high). Then signals in the two bands were independently reconstructed, which reduces noise, especially in reconstruction of high-frequency signals. The two bands were frequency-equalized [3], then the low band was displayed on the red channel of an RGB image, while the high band was displayed on the green channel of the same image. Therefore, smaller vessels appear in green and larger vessels appear in red.

B. Motion Correction Algorithm

To apply the motion correction algorithm, first the RSOM sinogram was acquired in the normal raster scan fashion. Then a 2D function from the acquired sinogram was calculated. We termed this 2D function the cumulative cross-correlation surface (CS):

$$cs(x_i, y_N) = \sum_{j=1}^{N-1} cs(x_i, y_j) + \left(\sum_{k,i} b(t_k, x_i^l, y_N) b(t_{k-d}, x_i^l, y_{N+1})\right) \quad (2)$$

where x_i and y_j are the positions of the acquisition grid in the fast-scanning axis and the slow-scanning axis [11]. Each pair (x_i, y_j) defines the position of an A-line within the sinogram and t_k are the time points of each A-line. The term $b(t_k, x_i^l, y_j)$ corresponds to the section of a B-plane where the A-lines range from the coordinates $\left(t_k, x_{i-\frac{1}{2}}, y_j\right)$ to the coordinates $(t_k, x_{i+l/2}, y_j)$. Fig. 2a shows a sinogram corresponding to the data acquired from the forearm of a subject and the parameters defined for the calculation of CS. We observed that when motion affected the sinogram, it also affected the continuity of the CS function. The motion correction algorithm works by calculating a synthetic smooth CS function and assuming that the vertical displacements can be quantified for every line of the sinogram as the reciprocal distance between the synthetic CS and the original CS. Once the vertical displacements are calculated, the images can be reconstructed taking into account the actual distances from the detector to the skin.

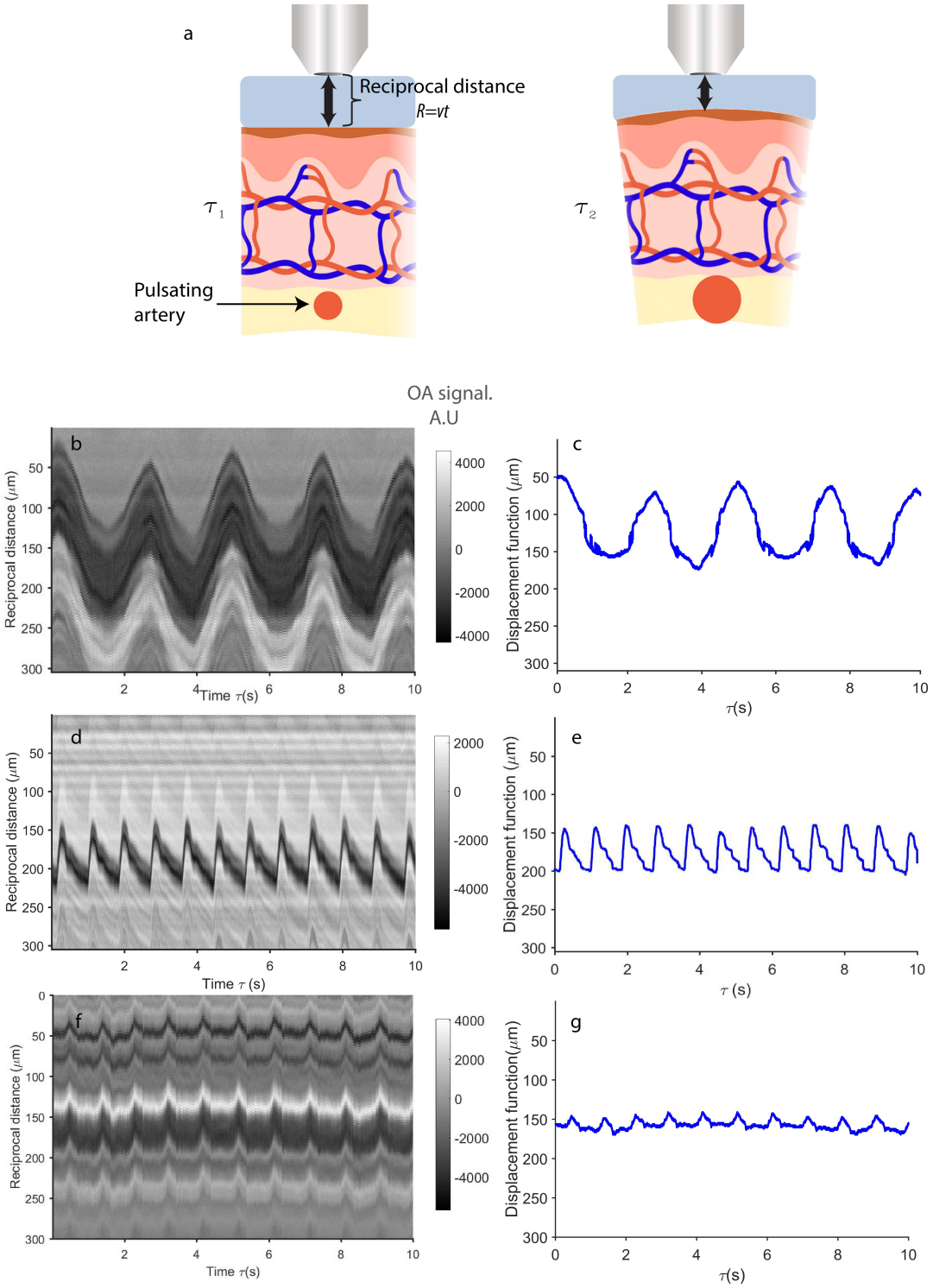

Fig. 1. **Quantitation of motion during RSOM scanning of different body parts of a healthy volunteer.** (a) Schematic of the measurement at two time points, during which motion occurs, such that the reciprocal distance decreases. For each site on the skin, motion graphs (*left column*) and displacement functions (*right column*) are shown for (b-c) the back, (d-e) volar aspect of the wrist, and (f-g) skin over the heart.

The motion correction algorithm was applied to the acquired data sets and its merits quantified. We selected the signal-to-noise ratio (SNR) as a figure of merit to compare the reconstructed images before and after motion correction. We defined SNR as

$$SNR(z) = \frac{< I(z) >}{\sigma(\epsilon)} \tag{3}$$

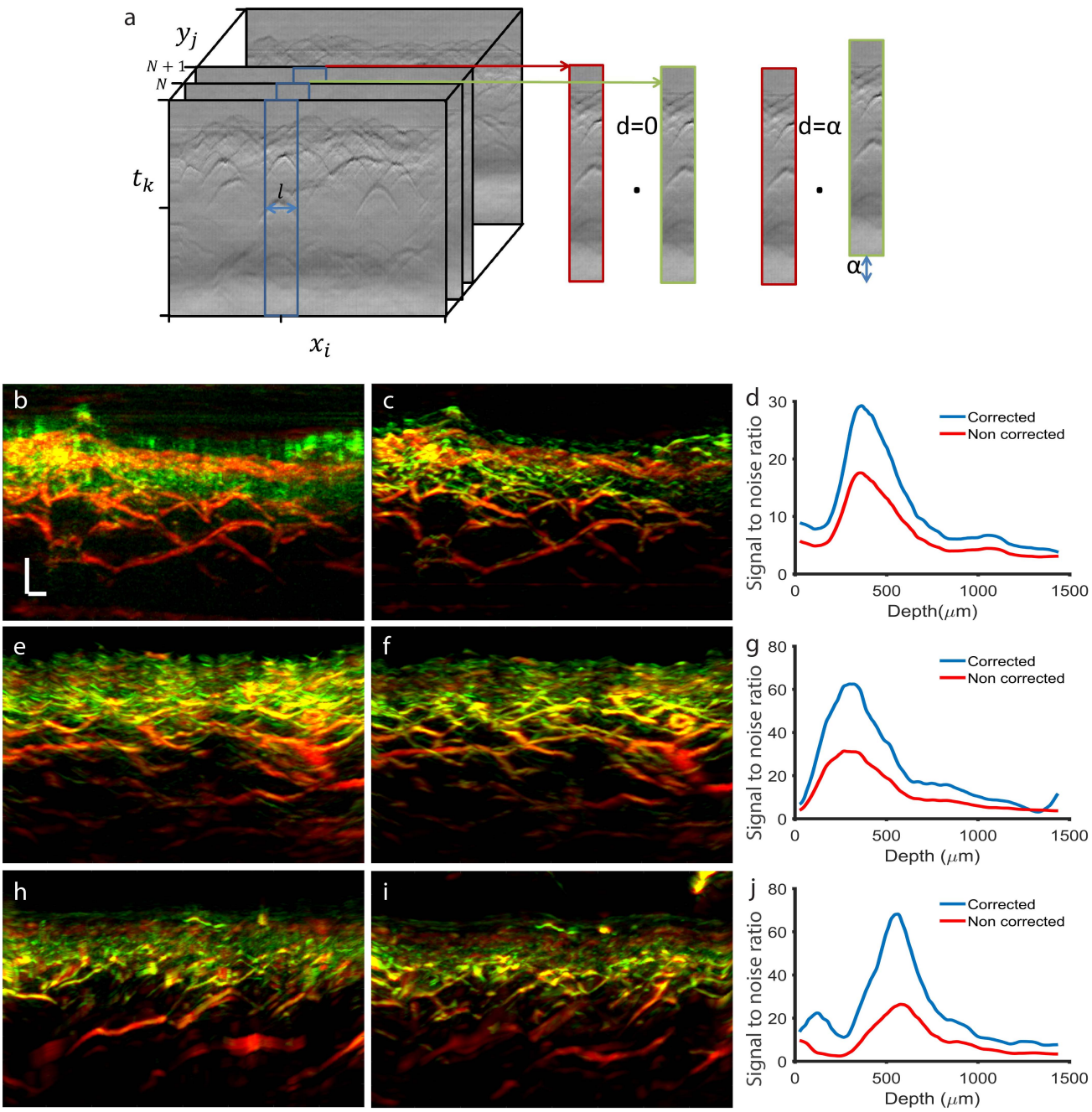

Fig. 2. **Validation of the proposed motion correction algorithm for RSOM imaging of skin subjected to different magnitudes of vertical displacement during scanning.** (a) Representation of a 3D sinogram depicting the parameters of (2). Image reconstructions are shown before motion correction (*left column*) and after motion correction (*middle column*), together with quantitation of SNR (3) in the two cases (*right column*) for (b-d) the lower arm, corresponding to a skin region experiencing low motion; (e-g) the upper arm, corresponding to medium motion; and (h-j) the back, corresponding to high motion. To make the algorithm work for imaging the back, data were acquired in 15-sec scanning sessions, which were then stitched together into a sinogram. Scale bars: 200 μm.

where $< I(z) >$ is the mean intensity of non-noisy values of a cuboid section of the reconstructed image. In the present study, the cuboid size was 4×2 mm with respect to the x and y axes. Its thickness was 120 μm and it was centered along the z direction. ϵ refers to a region of the reconstructed image with only noise and $\sigma(\epsilon)$ is the standard deviation.

To apply the algorithm to high-motion areas, the data acquisition process was modified. Data were acquired in discrete scanning sessions lasting 15 sec each. The volunteer was asked to hold his breath during each scanning session. Between sessions, the patient was allowed to breathe normally until he felt comfortable, at which point the next session was started. The data from the individual scanning sessions were stitched together to generate the sinogram. From this "stitched sinogram" the CS function was calculated using (2), and the subsequent steps of the standard motion correction algorithm were applied.

In order to test the motion correction algorithms, data were acquired over a skin region of 4×2 mm in the lower arm, shoulder and back of healthy volunteers and reconstructed

before and after applying motion correction on a cubic grid of $4 \times 2 \times 1.5$ mm using frequency equalization as described [3]. The values of l in (2) varied between 1 and 10. The improvement on the reconstructed images was calculated using 3.

In order to confirm that the motion correction algorithm works for complex motion patterns, we obtained the displacement function at several places of the body featuring a mixture of cardiac, breathing and random motion. We followed the approach described in Section A of Methods. We delayed the A-lines on motionless RSOM sinograms by the previously obtained displacements, then we applied the motion correction algorithm as described above to obtain the corrected images as well as estimated displacements. These estimated displacements were then compared with the displacements added to the sinogram.

III. Results

A. Measuring the Vertical Motion of the Skin

In Fig. 1, we summarize the results of the measurements of the vertical skin displacements.

We identified three sources of vertical displacements. The first one was breathing, which was observed in the DF function corresponding to the back and the upper part of the higher extremities (Fig. 1b,c). The second source of displacement was arterial pulsation, which was detected during scanning of the wrist area as micron-sized displacements in the tissue situated above the arteries (Fig. 1d,e). The shape of the DF function was the same as graphs obtained by classic photoplethismography [16] or tonometry [17]. The third source of vertical displacement was due to the beating heart, which created micron-sized vertical displacements of the skin over the heart (chest, Erb's point) during acquisition while the subject was holding his breath (Fig.1 f,g). The shape of the graph at Erb's point resembles the left ventricle volume of the Wiggers diagram [18], and the different phases of the systole and diastole can be distinguished. Such a graph is equivalent to an apex cardiogram [19].

The obtained mean motion values for different body parts were: 5 ± 3 μm (lower limbs), 3 ± 2 μm (lower arm), 15 ± 7 μm (upper arm), 17 ± 4 μm (upper leg), 94 ± 18 μm (back), and 110 ± 21 μm (chest). As expected, the amount of vertical motion increased with proximity to the chest, reflecting breathing. Based on the observed magnitude of vertical motion, the chest and abdomen were classified as "high-motion areas," the upper extremities as "medium-motion areas" and the lower part of the upper extremities and lower extremity as "low-motion areas." An exception was the volar aspect of the wrist, in which the arterial pulse created very strong motion.

B. Motion Correction Algorithm

In Fig. 2 we show the effect of the motion correction algorithm on the reconstructed images.

In Fig. 2b and Fig. 2c we show the reconstruction of an area of low motion in a healthy subject. By simple visual inspection one can easily observe the improvements in the quality of the image in terms of blurring and definition of the smallest vessels near the epidermis. The SNR clearly improved after motion correction (Fig. 2d). Similarly the motion correction strongly enhanced SNR in the medium-motion area (Fig. 2e,f,g).

The motion correction algorithm using data collected in the standard, continuous format consistently improved the SNR at least 2-fold in the low- and medium-motion areas. However, it did not clearly improve SNR in the high-motion areas (data not shown). In these cases, applying the algorithm to data acquired in discrete breathing sessions did produce a clear improvement. In Fig. 2 h,i,j we show the reconstruction of the back of a healthy subject, before and after motion correction based on data acquired in discrete breathing sessions. The motion correction visibly improved SNR.

In Fig. 3, we show a representative example of how the motion correction algorithm can deal with complex motion patterns. Fig. 3a-c compare the complex vertical displacement pattern added to a motionless sinogram with the estimated displacement obtained after applying the motion correction algorithm. The displacements are retrieved with excellent fidelity. As expected, the reconstructed images show quite poor quality before motion correction and much better quality afterwards (Fig 3d, e).

IV. Discussion

We have studied quantitatively, for the first time, the vertical motion of the skin affecting the quality of RSOM imaging. We have proposed an automated motion correction algorithm that can be used with skin regions experiencing low or moderate vertical displacement, and we modified the algorithm for skin areas subject to strong displacement. The algorithm clearly improves the quality of RSOM images including those taken on the back, where most melanomas develop. This motion correction algorithm may substantially improve the reliability of RSOM for imaging the skin and may finally allow the technique's full clinical potential to be realized [12]. Another motion correction algorithm conceived for optoacoustic imaging systems operates with several reconstructed frames acquired at the same transducer position [20], using maximum interposition correlation schemes. Our attempts with this approach led to sinogram deformation and ultimately low-quality reconstructed images (data not shown). This strategy may be applicable to RSOM if several A-lines were acquired at each scanning point, but this would prolong acquisition time from a few minutes to several hours. Another important difference is that previous algorithms have as input reconstructed frames, where in RSOM the input are raw A-lines.

To the best of our knowledge, this is the first report of the magnitude of vertical motion that affects RSOM at different skin sites. Prior work [11] indicated that motion due to breathing exists, but it was not quantified. Moreover, here we demonstrated that there are two other sources of vertical displacement: arterial pulsation and the heartbeat. The graphs obtained from the chest area above the heart (Erb's point) correspond to apex cardiograms [19], which complement other cardiac sensing methods that provide different information regarding the heart beat, including ballistocardiography [21], electrocardiography [22], laser Doppler vibrometry [23] or phonocardiography [24].

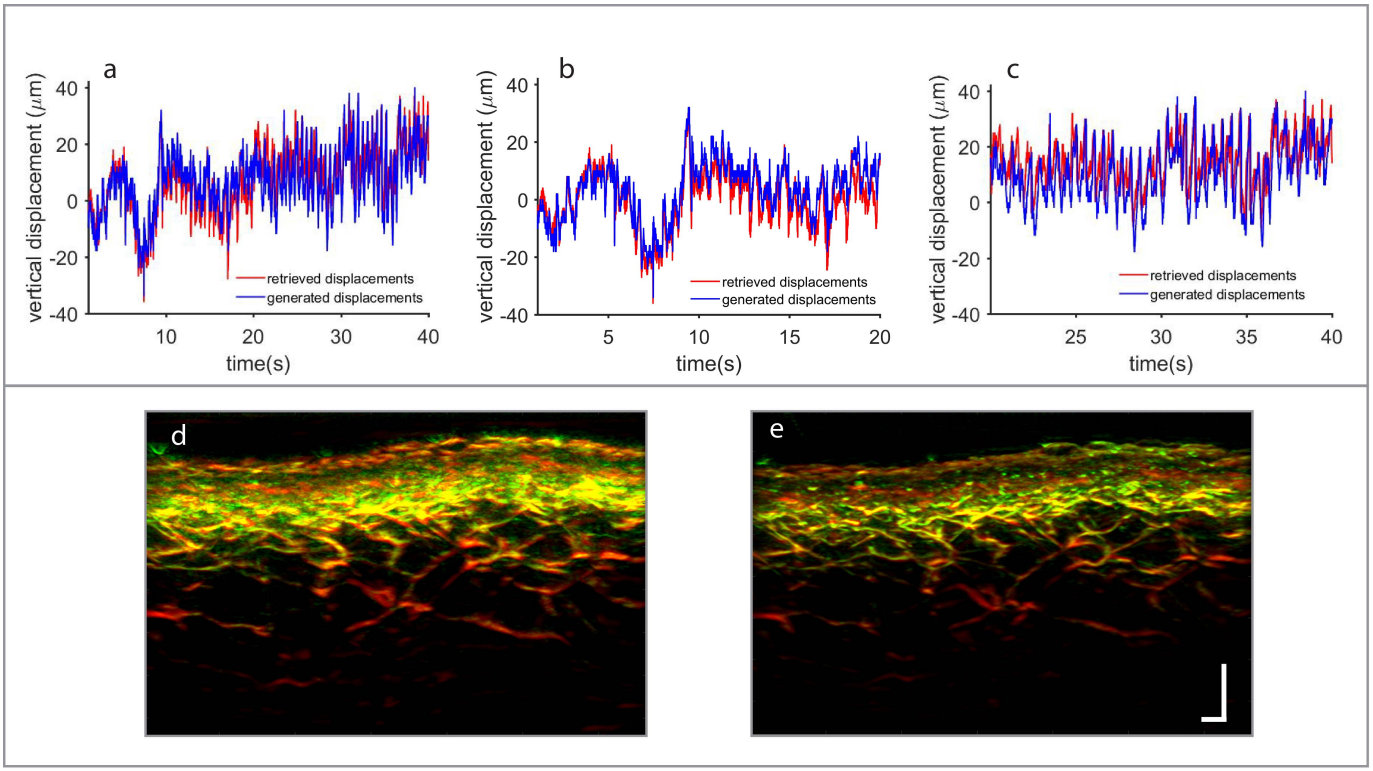

Fig. 3. **Validation of the proposed motion correction for complex motion patterns** a) blue: displacement function measured on the inside bend of the elbow, where pulse, breathing and also random motion is expected. Such motion was afterward introduced in a motionless sinogram. red: displacement function retrieved by the motion correction algorithm from the perturbed sinogram. b) figure shown in a, zoomed. c) figure shown in a, zoomed. d) reconstructed image after adding motion to the sinogram, without motion correction. e) reconstructed image after motion correction.

When measuring the skin motion in the wrist we obtained the same graph that is obtained by photoplethismography [16] or tonometry [17] and is due to pulsation of the radial artery. The same kind of motion can be observed in locations in which there are superficial pulsating arteries, such as in the tibialis anterior region containing the arteria tibialis (data not shown).

When applying the motion correction algorithm to standard RSOM data, the displacement function can be obtained, as shown in Fig 3. Cardiac or breathing motion can be extracted from this displacement function, using spectral analysis for example. In this way, RSOM can be applied beyond imaging to provide real-time biomechanical and functional information.

The motion correction algorithm clearly improved image quality at all body sites were it was tested. The maximum improvement was obtained for the dermal areas, where the smallest capillaries of the skin lie. This is not surprising given that such capillaries have a diameter around 10 μm [25], which is on the order of the motion measured in low-motion areas (lower limbs, 5±3 μm; lower arm, 3±2 μm), considerably less than the motion in medium-motion areas (upper arm, 15±7 μm; upper leg, 17±4 μm), and one order of magnitude less than the motion observed in high-motion areas. Imaging of venules and arterioles in the dermis are less affected by motion since their size ranges from 20 μm to 100 μm [25]. Although the modified motion correction clearly improved SNR in high-motion areas, the overall improvement in image quality was not as great as in areas of low or medium motion. Further refinement of the algorithm should take this into account. Furthermore, when imaging melanomas, other challenges must be addressed, like the shading effects that may occur due to strong absorption of the excitation light at the surface of lesion. It may be necessary to use longer wavelengths (e.g. 650 nm) at which melanin absorbs less.

The algorithm was tested here only with single-wavelength RSOM data. It is also likely to benefit multispectral optoacoustic mesoscopy (MOM) [6], where its application should be straightforward.

The data currently available do not allow quantitative comparison between the algorithm presented here and the one presented by Schwarz *et al.* [11], since the two studies used different figures of merit. Nevertheless, the algorithm presented here shows two clear advantages [11] over the previous one: it does not rely on segmentation methods, which may not be feasible for certain imaging contexts; and it is fully automated.

In order to be deployed in the clinic, RSOM must be a robust technique. Therefore, understanding motion and being able to correct for it automatically are essential for its clinical translation. This paper clarifies the origin and magnitude of motion in RSOM while describing an automated motion correction algorithm that will help RSOM fulfill its clinical promise.

ACKNOWLEDGMENT

J Aguirre would like to thank Dr. J.C. Baracchi for useful discussions.

REFERENCES

[1] J. Aguirre, M. Schwarz, D. Soliman, A. Buehler, M. Omar, and V. Ntziachristos, "Broadband mesoscopic optoacoustic tomography reveals skin layers," *Opt. Lett.*, vol. 39, no. 21, pp. 6297–6300, Nov. 2014.

[2] M. Schwarz, M. Omar, A. Buehler, J. Aguirre, and V. Ntziachristos, "Implications of ultrasound frequency in optoacoustic mesoscopy of the skin," *IEEE Trans. Med. Imag.*, vol. 34, no. 2, pp. 672–677, Feb. 2015.

[3] J. Aguirre *et al.*, "Precision assessment of label-free psoriasis biomarkers with ultra-broadband optoacoustic mesoscopy," *Nature Biomed. Eng.*, vol. 1, May 2017, Art. no. 0068.

[4] J. Aguirre *et al.*, "Assessing nailfold microvascular structure with ultra-wideband raster-scan optoacoustic mesoscopy," *Photoacoustics*, vol. 10, pp. 31–37, Jun. 2018.

[5] M. Omar, J. Gateau, and V. Ntziachristos, "Raster-scan optoacoustic mesoscopy in the 25-125 MHz range," *Opt. Lett.*, vol. 38, no. 14, pp. 2472–2474, Jul. 2013.

[6] M. Schwarz, A. Buehler, J. Aguirre, and V. Ntziachristos, "Three-dimensional multispectral optoacoustic mesoscopy reveals melanin and blood oxygenation in human skin *in vivo*," *J. Biophoton.*, vol. 9, nos. 1–2, pp. 55–60, Jan. 2016.

[7] X. L. Deán-Ben, H. López-Schier, and D. Razansky, "Optoacoustic micro-tomography at 100 volumes per second," *Sci. Rep.*, vol. 7, no. 1, Jul. 2017, Art. no. 6850.

[8] A. A. Plumb, N. T. Huynh, J. Guggenheim, E. Zhang, and P. Beard, "Rapid volumetric photoacoustic tomographic imaging with a Fabry-Perot ultrasound sensor depicts peripheral arteries and microvascular vasomotor responses to thermal stimuli," *Eur. Radiol.* vol. 28, no. 3, pp. 1037–1045, Mar. 2018.

[9] M. Omar, D. Soliman, J. Gateau, and V. Ntziachristos, "Ultrawideband reflection-mode optoacoustic mesoscopy," *Opt. Lett.*, vol. 39, no. 13, pp. 3911–3914, Jul. 2014.

[10] M. Schwarz *et al.*, "Optoacoustic dermoscopy of the human skin: Tuning excitation energy for optimal detection bandwidth with fast and deep imaging *in vivo*," *IEEE Trans. Med. Imag.*, vol. 36, no. 6, pp. 1287–1296, Jun. 2017.

[11] M. Schwarz, N. Garzorz-Stark, K. Eyerich, J. Aguirre, and V. Ntziachristos, "Motion correction in optoacoustic mesoscopy," *Sci. Rep.*, vol. 7, no. 1, Sep. 2017, Art. no. 10386.

[12] H. Lev-Tov, "Dive deep, stay focused!" *Sci. Transl. Med.*, vol. 9, no. 391, eaan4292, May 2017.

[13] A. Green, "A theory of site distribution of melanomas: Queensland, Australia," *Cancer Causes Control*, vol. 3, no. 6, pp. 513–516, Nov. 1992.

[14] K. H. Chiappa and A. H. Ropper, "Evoked potentials in clinical medicine," *New England J. Med.*, vol. 306, no. 20, pp. 1205–1211, May 1982.

[15] H. Barquero, S. Crozat, and G. Pierre, "Development of large aperture, high-frequency piezo-electric transducers for photoacoustic imaging," in *Proc. IEEE Int. Ultrason. Symp. (IUS)*, Sep. 2017, pp. 1–4.

[16] J. Allen, "Photoplethysmography and its application in clinical physiological measurement," *Physiological Meas.*, vol. 28, no. 3, pp. R1–R39, Mar. 2007.

[17] C.-H. Chen *et al.*, "Estimation of central aortic pressure waveform by mathematical transformation of radial tonometry pressure. Validation of generalized transfer function," *Circulation* vol. 95, no. 7, pp. 1827–1836, Apr. 1997.

[18] J. R. Mitchell and J.-J. Wang, "Expanding application of the Wiggers diagram to teach cardiovascular physiology," *Adv. Physiol. Educ.*, vol. 38, no. 2, pp. 170–175, Jun. 2014.

[19] E. Tafur, L. S. Cohen, and H. D. Levine, "The normal apex cardiogram: Its temporal relationship to electrical, acoustic, and mechanical cardiac events," *Circulation*, vol. 30, no. 3, pp. 381–391, Sep. 1964.

[20] T. F. Fehm, X. L. Deán-Ben, S. J. Ford, and D. Razansky, "*In vivo* whole-body optoacoustic scanner with real-time volumetric imaging capacity," *Optica*, vol. 3, no. 11, pp. 1153–1159, Nov. 2016.

[21] T. Koivistoinen, S. Junnila, A. Värri, and T. Kööbi, "A new method for measuring the ballistocardiogram using EMFi sensors in a normal chair," in *Proc. 26th Annu. Int. Conf. IEEE Eng. Med. Biol. Soc.*, vol. 1, Sep. 2004, pp. 2026–2029.

[22] N. J. Holter, "New method for heart studies: Continuous electrocardiography of active subjects over long periods is now practical," *Science*, vol. 134, no. 3486, pp. 1214–1220, Oct. 1961.

[23] P. Castellini, M. Martarelli, and E. P. Tomasini, "Laser Doppler vibrometry: Development of advanced solutions answering to technology's needs," *Mech. Syst. Signal Process.*, vol. 20, no. 6, pp. 1265–1285, Aug. 2006.

[24] S. Tanaka, Y. Matsumoto, and K. Wakimoto, "Unconstrained and non-invasive measurement of heart-beat and respiration periods using a phonocardiographic sensor," *Med. Biol. Eng. Comput.*, vol. 40, no. 2, pp. 246–252, Mar. 2002.

[25] I. M. Braverman, "The cutaneous microcirculation: Ultrastructure and microanatomical organization," *Microcirculation*, vol. 4, no. 3, pp. 329–340, Sep. 1997.